

Biexponential Diffusion Tensor Analysis of Human Brain Diffusion Data

Stephan E. Maier,^{1*} Sridhar Vajapeyam,² Hatsuho Mamata,¹ Carl-Fredrik Westin,¹ Ferenc A. Jolesz,¹ and Robert V. Mulkern²

Several studies have shown that in tissues over an extended range of b -factors, the signal decay deviates significantly from the basic monoexponential model. The true nature of this departure has to date not been identified. For the current study, line scan diffusion images of brain suitable for biexponential diffusion tensor analysis were acquired in normal subjects on a clinical MR system. For each of six noncollinear directions, 32 images with b -factors ranging from 5 to 5000 s/mm² were collected. Biexponential fits yielded parameter maps for a fast and a slow diffusion component. A subset of the diffusion data, consisting of the images obtained at the conventional range of b -factors between 5 and 972 s/mm², was used for monoexponential diffusion tensor analysis. Fractional anisotropy (FA) of the fast-diffusion component and the monoexponential fit exhibited no significant difference. FA of the slow-diffusion biexponential component was significantly higher, particularly in areas of lower fiber density. The principal diffusion directions for the two biexponential components and the monoexponential solution were largely the same and in agreement with known fiber tracts. The second and third diffusion eigenvector directions also appeared to be aligned, but they exhibited significant deviations in localized areas. *Magn Reson Med* 51: 321–330, 2004. © 2004 Wiley-Liss, Inc.

Key words: diffusion tensor imaging; line scan; high- b diffusion imaging; white matter; biexponential signal decay

Routine diffusion imaging of the brain generally utilizes b -factors within a range of 0–1000 s/mm². Apparent diffusion coefficient (ADC) maps are then generated assuming that the relationship between the MR signal and the b -factor is monoexponential. However, it has been shown that for rat brain the signal decay with b -factors over an extended range of up to 10000 s/mm² is better described with a biexponential curve (1). Similar findings were made for normal human brain, using multiple b -factors of up to 6000 s/mm² (2–4).

For the conventional range of b -factors, the sensitivity of the ADC value to the direction of the diffusion sensitization gradient in some parts of the brain is well recognized and attributed to anisotropic diffusion along myelinated

axons in the white matter. With this well-established model, measurement of the ADC value for six noncollinear directions suffices to yield a theoretically complete description of the full diffusion tensor for each voxel sampled (5). One might expect that the biexponential model is readily extended to include the diffusion tensor formalism. Earlier in vivo studies, which were based on the analysis of only two or three orthogonal diffusion directions, indeed revealed that directional dependence also applies to each component in the biexponential model (3, 6, 7). The limited number of directions sampled, however, did not permit computation of anisotropy or eigenvector direction. To date, only estimates have been published for the biexponential diffusion tensor in normal human brain (8). Integral biexponential diffusion tensor data analysis has been employed in animal experiments conducted at very high magnetic field strengths [9–11]. It can be expected that the findings are strongly influenced by tissue viability and temperature, and field-strength-dependent relaxation times, as well as by the diffusion encoding and echo times (TEs) that can be attained with a particular gradient hardware. Since diffusion tensor imaging (DTI) is most widely employed in the human brain and on clinical MR systems, exploration of the biexponential diffusion tensor properties under comparable experimental conditions is important in order to put the findings into a wider clinical context.

In the present study (12), human brain image data suitable for biexponential diffusion tensor analysis were acquired in normal subjects on a clinical MR system. For each diffusion component, maps of anisotropy and eigenvectors were computed. For reference purposes, a subset of the data was used for a conventional, monoexponential diffusion tensor analysis.

MATERIALS AND METHODS

MR Diffusion Imaging

Diffusion-weighted images for a wide range of b -factors were obtained with a line scan diffusion imaging (LSDI) sequence. Details about this single-shot column sampling technique, which is distinguished by minimal motion sensitivity and reduced artifacts in areas exhibiting large variations in susceptibility, have been published previously [13–15]. The LSDI sequence was implemented on a 1.5 Tesla LX Echospeed whole-body system (General Electric Medical Systems, Milwaukee, WI) with version 8.2.5 software release. This system permits a maximum gradient strength of up to 40 mT/m. The standard birdcage head coil was used, and neither cardiac gating nor head restraints were employed. Four healthy male volunteers (mean age 36 years) were scanned after they provided

¹Department of Radiology, Brigham and Women's Hospital, Boston, Massachusetts.

²Department of Radiology, Children's Hospital, Harvard Medical School, Boston, Massachusetts.

Presented in part at the 9th annual meeting of ISMRM, Glasgow, Scotland, 2001.

Grant sponsor: NIH; Grant number: 1R01 NS39335; Grant sponsor: NATO; Grant number: LST CLG 976686.

*Correspondence to: Stephan E. Maier, M.D., Ph.D., Radiology (MRI), Brigham and Women's Hospital, Harvard Medical School, 75 Francis St., Boston, MA 02115. E-mail: stephan@bwh.harvard.edu

Received 27 March 2003; revised 29 August 2003; accepted 30 August 2003.

DOI 10.1002/mrm.10685

Published online in Wiley InterScience (www.interscience.wiley.com).

© 2004 Wiley-Liss, Inc.

informed consent. All studies were conducted within the guidelines of the institutional internal review board (IRB).

Thirty-two images with linearly increasing diffusion weighting between 5 and 5000 s/mm² were acquired for each of six noncollinear diffusion directions ((1,1,0), (0,1,1), (1,0,1), (0,1,-1), (1,-1,0), (-1,0,1)). The diffusion-encoding times δ and Δ were held constant at 35 ms and 47 ms, respectively. In each subject a single axial section at the level of the lateral ventricles was scanned. Image geometry was given by an effective (13) section thickness of 6 mm, a rectangular field of view (FOV) of 220 × 165 mm, and a matrix size of 64 × 48 columns, interpolated to a final image matrix of 256 × 192 with zero-filling in the frequency domain along the frequency-encode direction, and with spline interpolation between lines. During preliminary experiments, it was found that for the tissues of interest, this image geometry together with a receiver bandwidth of ±2.23 kHz produced unaveraged signals well above the noise threshold for all combinations of diffusion-encoding directions and b -factors used.

The TE was 94 ms and the time interval between column excitations was 155 ms. This timing permitted an effective (13) repetition time (TR) of 2635 ms and a total scan time of 27 min for a single slice and one excitation. It should be emphasized that the diffusion gradient amplitudes used exploited only 70% of the maximal permissible gradient amplitude. Due to gradient heating limitations, the reduced gradient amplitude permitted a considerably shorter interval between column excitations, and ultimately a reduced scan time with only a modest increase in TE. With further reduction, the TR would not have been duty cycle limited, but rather determined by the TE needed to accommodate the imaging and diffusion-encoding gradients.

Data Analysis

Data analysis was performed offline on a Linux personal computer using software written by the authors in C programming language. A nonlinear least-squares Levenberg-Marquardt algorithm was employed for each pixel to fit brain signal intensity decay S with diffusion-weighting b to a biexponential function of the form

$$S = A_f \exp(-D_f b) + A_s \exp(-D_s b) \quad [1]$$

where D_f and D_s are the ADCs of a fast and a slow diffusion component, respectively, and A_f and A_s are their respective sizes. It was assumed that both D_f and D_s vary with the diffusion-encoding direction and, as in the case of monoexponential diffusion-related signal loss, can be represented as tensor components. For the component sizes A_f and A_s , the diffusion direction dependence is not obvious. Therefore, two fitting strategies were studied: one with and one without diffusion direction dependence of A_f and A_s . For the approach with diffusion direction dependence, A_f and A_s , together with D_f and D_s , were assumed to be tensor components and were assessed by independent fits for each diffusion direction. For the second approach, A_f and A_s were treated as constants and were obtained by a fit of a composite decay curve generated by the geometric average of the measures along the different diffusion-encoding

directions, i.e., $\sqrt[6]{S_1 S_2 S_3 S_4 S_5 S_6}$ for the six directions of the tensor configuration. These were then used to determine D_f and D_s in separate fits for each of the different diffusion-encoding directions. The two fitting approaches to the signal decay S_k for each gradient direction with unit vector $\hat{\mathbf{g}}_k$, can be differentiated on a mathematical basis with the following two equations:

$$S_k = \hat{\mathbf{g}}_k^T \mathbf{A}_f \hat{\mathbf{g}}_k \exp[-b(\hat{\mathbf{g}}_k^T \mathbf{D}_f \hat{\mathbf{g}}_k)] + \hat{\mathbf{g}}_k^T \mathbf{A}_s \hat{\mathbf{g}}_k \exp[-b(\hat{\mathbf{g}}_k^T \mathbf{D}_s \hat{\mathbf{g}}_k)] \quad (\text{unconstrained fit}) \quad [2]$$

$$S_k = A_f \exp[-b(\hat{\mathbf{g}}_k^T \mathbf{D}_f \hat{\mathbf{g}}_k)] + A_s \exp[-b(\hat{\mathbf{g}}_k^T \mathbf{D}_s \hat{\mathbf{g}}_k)] \quad (\text{constrained fit}) \quad [3]$$

Subsequent diagonalization produced respective eigenvalues ($\lambda_1, \lambda_2, \lambda_3$) and eigenvectors of each tensor. The three diffusion eigenvalues were used to compute trace ADC and the dimensionless fractional anisotropy (FA) (16) of the fast- and slow-diffusion components:

$$FA = \frac{\sqrt{(\lambda_1 - \lambda_2)^2 + (\lambda_2 - \lambda_3)^2 + (\lambda_1 - \lambda_3)^2}}{\sqrt{2} \sqrt{\lambda_1^2 + \lambda_2^2 + \lambda_3^2}} \quad [4]$$

Data points were only included in the fit if their signal exceeded three times the noise baseline. As already indicated, MRI parameters were chosen so that independently of the diffusion-encoding direction, the signal of all tissues of interest was above this threshold for the entire range of b -factors applied. The quality of the fit was judged on the basis of the χ^2 error, i.e., the sum of the unweighted squared differences between the input data points and the function values, evaluated at the same b -factors. The χ^2 error merit function may contain several local minima. To improve the chances of finding the global optimum of the fit function, starting values for D_f and D_s were varied incrementally over a relatively wide range. Processing time for a complete data set was on the order of minutes.

A subset of the diffusion data, consisting of the images obtained at the conventional range of b -factors between 5 and 972 s/mm² (i.e., seven images for each diffusion-encoding direction) was fitted monoexponentially with the same nonlinear least-squares Levenberg-Marquardt method. The resulting diffusion tensor was also diagonalized in order to obtain eigenvectors, eigenvalues, and the associated FA as reliable measures of reference.

To compare directions of the principal axes of diffusion among the two components of the biexponential fit and the single component of the monoexponential fit, the deviation angle φ was determined from the eigenvectors of interest \mathbf{a} and \mathbf{b} with the expression

$$\varphi = \arccos(\mathbf{a} \cdot \mathbf{b}) \quad [5]$$

which produces φ values in the range of 0–180°. The distribution of these deviation angles was then determined. One distribution included data from all pixels where the FA of the diffusion determined with a monoexponential fit was > 0.4 (i.e., mostly very dense fiber tracts, such as the corpus callosum and internal capsule). A sec-

ond distribution included data from all pixels where the monoexponential FA was ≤ 0.4 , but > 0.2 (i.e., it included more peripheral white matter tracts but no gray matter). Tissues outside the brain were excluded from the distribution by a manually drawn region of interest (ROI).

In order to describe the distribution of φ analytically, a polar coordinate system is considered, where the latitude angle follows a normal distribution and the longitude angle is evenly distributed. The distribution can consequently be described by a normal probability density function adjusted by a sine function. Accordingly, the equation

$$f(\varphi) = \sin(|\varphi - \delta|) \frac{s}{\sigma \sqrt{2\pi}} \exp\left[-\frac{(\varphi - \delta)^2}{2\sigma^2}\right] \quad [6]$$

where σ is the standard deviation (SD) of the normal distribution, δ is a potentially present angle bias, and s is a scaling factor that normalizes the distribution, was fitted for a range of 0° – 30° with the Levenberg-Marquardt algorithm to the histogram of the angle deviations.

Maps of the various parameters (i.e., trace ADC, FA, fast diffusion component signal fraction $A_f/(A_f + A_s)$, φ , and χ^2) were used for ROI analysis. It was confirmed that spatial interpolation of the diffusion data, which was performed to facilitate the placement of ROIs, did not introduce any systematic errors. ROIs were manually drawn within the medial portion of the posterior corpus callosum, the left internal capsule, and the left thalamus. The size of the manually drawn ROIs at original scan resolution was 3–5 pixels. This rather small size (in comparison to the structures measured) was used to minimize partial volume effects due to low resolution and possible head displacement during the long scan. For each particular ROI, the same contour was used for all of the subjects, with repositioning as needed. A two-sided Student's t -test was applied to confirm statistically significant differences, whereby a P value of < 0.05 was considered significant.

RESULTS

Diffusion-weighted images over a wider b -factor range than typically used were successfully obtained in all volunteers. The diffusion-related signal decay demonstrated a marked directional dependence. Typical signal decays of an individual pixel located in white matter, together with their respective fits, are shown in Fig. 1.

ADC

Figure 2 shows an example of diffusion-weighted images and corresponding computed ADC maps for the fast- and slow-diffusion components. As summarized in Table 1, the resulting trace ADCs were biexponential for all three ROIs investigated and differed little between the two fitting methods used. The constrained fit when compared with the unconstrained fit produced on average a 4.4% ($0.054 \mu\text{m}^2/\text{ms}$) lower value for the fast-diffusion component and a 9.7% ($0.017 \mu\text{m}^2/\text{ms}$) higher value for the slow-diffusion component. The quality of fit, as expressed with the χ^2 error parameter, was slightly worse (on average, 12.4%) for the constrained fit than for the uncon-

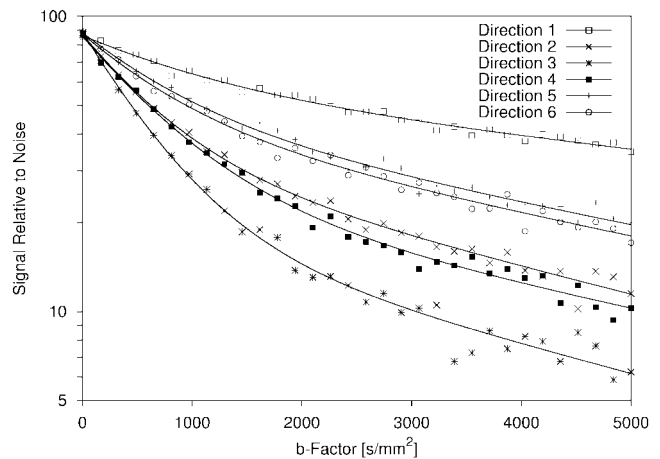


FIG. 1. Logarithmic plot of MR signal intensities relative to noise vs. b -factor along different diffusion-encoding directions (see Materials and Methods section) for an individual pixel located within the right internal capsule. Noise was also measured within a single pixel outside the subject's head. Along all directions the diffusion-related signal decay clearly deviates from a basic monoexponential decay. The solid curves represent the optimal biexponential fits.

strained fit. However, this difference appeared to be negligible in comparison to the χ^2 of a simple monoexponential fit, which for both fitting methods was up to a magnitude larger than the χ^2 of the corresponding biexponential fit. For the fitting method that constrained the component sizes, negative slow-diffusion component values were observed in areas of high anisotropy for encoding directions approximately perpendicular to the fiber. Negative values were not found for the trace ADC.

Component Sizes

Relative component sizes of the two fitting methods differed very little; on average, the relative component size extracted from the composite decay curve vs. the relative trace of the tensor component size for the unconstrained model, was 3.6% lower (Table 1). For the unconstrained fit, where the component sizes are treated as independent tensors, the primary eigenvector of the tensor component size of the slow-diffusion component was found to be largely orthogonal to the other three primary eigenvectors. This observation is documented in Fig. 3.

FA

Diffusion FA maps of the unconstrained fit presented organized structures in the area of the corpus callosum and internal capsule (Fig. 4a and b). More peripheral tracts, such as the optical tract, could not be distinguished and a more detailed analysis of the data was therefore not performed. Diffusion FA maps of the constrained fit revealed intricate details of fiber tract anatomy, comparable to FA maps that result from an experiment with a conventional range of b -factors and monoexponential fitting (see Fig. 4c–e). Notable for the FA map of the slow-diffusion component is the much higher anisotropy and the seemingly larger fraction of white matter tissue visualized. These findings are confirmed by the ROI measurements pre-

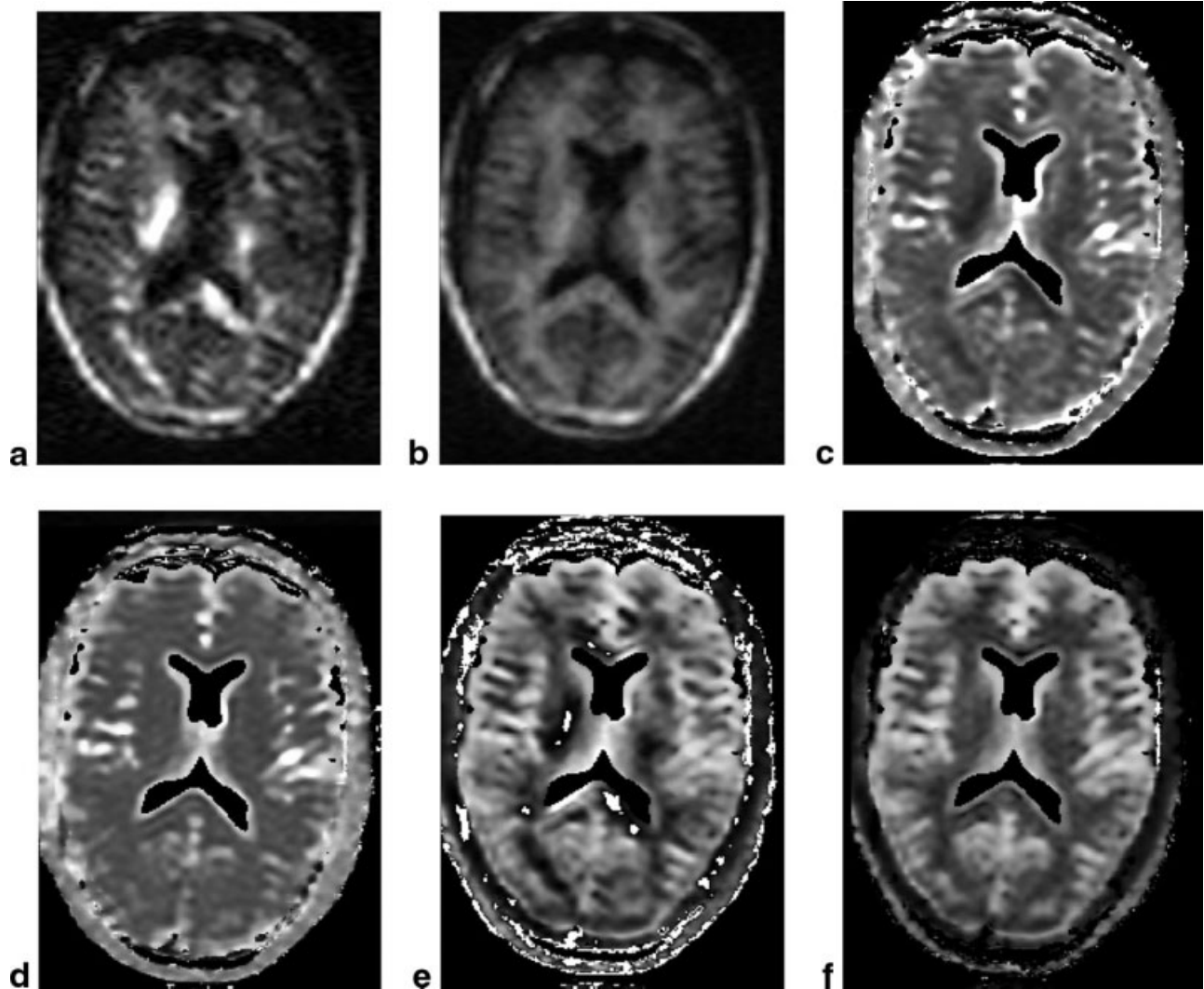


FIG. 2. Diffusion-weighted images and corresponding ADC maps of the fast- and slow-diffusion components. All of the ADC maps shown here were calculated according to the second fitting approach, where A_f and A_s are treated as constants (see Materials and Methods section). **a:** Diffusion-weighted image with diffusion weighting of 5000 s/mm^2 along $(1,1,0)$, (i.e., direction 1 in Fig. 1). **b:** Geometric average of six images with diffusion weighting of 5000 s/mm^2 along noncollinear directions. **c:** ADC map of the fast-diffusion component along $(1,1,0)$. White corresponds to an ADC value of $4.0 \mu\text{m}^2/\text{ms}$. Within white matter, the directional dependence of the ADC values is evident. The very high ADC values visible in some cerebrospinal fluid-filled spaces can most likely be attributed to partial volume effects in voxels located at the brain tissue surface. Areas with a monoexponential ADC value $> 2.0 \mu\text{m}^2/\text{ms}$ (such as the ventricles) have been masked. In these areas, where partial volume effects are less likely to play a role, the fast-component ADC was found to be less high, i.e., around $3.0 \mu\text{m}^2/\text{ms}$. **d:** Trace ADC map of the fast-diffusion component displayed with same scale as in **c**. **e:** ADC map of the slow-diffusion component along $(1,1,0)$. Within white matter, a very strong directional dependence of the ADC values is evident. White corresponds to an ADC value of $0.75 \mu\text{m}^2/\text{ms}$. Because of the aliased gray scale, negative values appear bright (bright spots within the left side of the corpus callosum and the right internal capsule). These areas appear to correspond with areas of minimal signal loss on the diffusion-weighted image shown in **a**. **f:** Trace ADC map of the slow-diffusion component displayed with same scale as in **e**.

sented in Table 2. In particular, the ratio of the fast-diffusion component FA vs. the FA of the monoexponential fit is close to one for all different ROIs investigated. On the other hand, the ratio of the slow-diffusion component FA vs. the FA of the monoexponential fit is significantly larger than one (e.g., as high as 1.4 in the corpus callosum). It appears to be even higher in areas of lower fiber density (e.g., 1.7 in the thalamus) (Table 2).

Eigenvector Directions

For the unconstrained fit, the first diffusion eigenvectors appeared to agree with the underlying anatomy. This

agreement, however, was limited to areas with very high anisotropy, such as the corpus callosum and internal capsule, and further analysis was therefore not pursued. In contrast, the constrained fit demonstrated excellent agreement with the underlying white matter anatomy for the entire section. As documented in Fig. 5 and Table 3, there was also excellent agreement between the fiber direction assessed with monoexponential fitting and the principal axes of diffusion of the two components determined with biexponential fitting using constrained component sizes. The agreement was best in the areas of highest fiber density (i.e., the corpus callosum) and worst in areas of low or

Table 1

Average Trace ADCs, Fast Diffusion Component Size Fraction, and Quality of Fit Measured With Two Different Fitting Methods Within Different Regions of Interest of Four Normal Volunteers

Region of interest		Corpus callosum	Internal capsule	Thalamus
ADC _f (μm ² /ms)	Unconstrained fit	1.288 (0.079)	1.215 (0.050)	1.175 (0.047)
	Constrained fit	1.176 (0.050)	1.201 (0.040)	1.139 (0.055)
ADC _s (μm ² /ms)	Unconstrained fit	0.162 (0.005)	0.162 (0.004)	0.233 (0.008)
	Constrained fit	0.195 (0.015)	0.176 (0.007)	0.237 (0.012)
A _f /(A _f + A _s)	Unconstrained fit	0.656 (0.041)	0.628 (0.017)	0.676 (0.025)
	Constrained fit	0.699 (0.046)	0.643 (0.014)	0.689 (0.028)
χ ² /χ ² _M	Unconstrained fit	0.393 (0.122)	0.102 (0.025)	0.150 (0.027)
	Constrained fit	0.427 (0.121)	0.121 (0.023)	0.165 (0.028)

ADC_f, trace ADC of fast diffusion component; ADC_s, trace ADC of slow diffusion component; χ²/χ²_M, χ² ratio of multi- vs. monoexponential fit (averaged over six directions); SD (N = 4) is given in parentheses.

absent fiber anisotropy (i.e., the thalamus or gray matter). Figure 6 provides an example of the distribution and associated fit of deviation angles between principal axes of diffusion. The SD σ and the bias δ of the adjusted normal distribution that was fitted to the angle difference histogram data are listed in Table 3. In agreement with the finding of the ROI analysis, the SD in areas of high fiber density or anisotropy was smaller than in areas of low fiber density or anisotropy. Finally, Fig. 7 shows a direct comparison between primary diffusion eigenvectors obtained with biexponential and monoexponential fitting.

For the second and third eigenvectors, a quantitative assessment of the deviation angle was not performed. However, visual inspection of the constrained solution data revealed that in the juxtacaudate area, as well as within the anterior and posterior parts of the corpus callosum, the second eigenvectors of the fast- and slow-diffusion components were largely orthogonal to each other. At the same time, none of them were parallel with the second eigenvector of the monoexponential fit (see Fig. 8). On the other hand, within the posterior limb of the internal capsule, second eigenvectors of the fast- and slow-

diffusion components, as well as the second eigenvector of the monoexponential fit, were consistently parallel to each other.

DISCUSSION

Although the directional dependence of the diffusion signal attenuation in human brain at very high b -factors has been observed previously [3, 7, 8], this is the first report that deals with the integral biexponential analysis of such human brain diffusion tensor data. Clark et al. (8) recently presented diffusion tensor data that were obtained at b -factors of up to 3500 s/mm². However, the data were obtained for only four diffusion-weighting levels, which prevented the authors from conducting a proper biexponential analysis. Instead, they analyzed the diffusion data with two separate monoexponential fits, i.e., one fit for the lower and one fit for the upper range of b -factors. This approach, while simple, does not reliably separate the fast- and slow-diffusion components, since both components contribute sizably over the entire range of diffusion weighting used by the authors. In general, as also pointed out in the paper by Clark et al. (8), this simplified model underestimates the ADC of the fast-diffusion component and overestimates the ADC of the slow-diffusion component. Only at even higher b -factors, where the influence of the fast-diffusion component tends to become negligible, can the slow-diffusion component be reliably computed with only a monoexponential fit.

Biexponential analysis of diffusion tensor data has previously been presented for excised rat spinal cord at room temperature (9), in vivo rat spinal cord (10), and perfused rat heart (11). All of these animal experiments were performed at very high field strengths of 7 and 14 Tesla. Therefore, the findings are not necessarily applicable to the observations made in the present study, which was conducted on a clinical system with only 1.5 Tesla field strength. In particular, the use of human subjects imposed practical limits on the scan time, which together with the lower field strength significantly reduced the available signal-to-noise ratio (SNR). Another important difference is the superior gradient performance of small-bore systems, which due to the considerably shorter diffusion-encoding and echo times may lead to different weighting of the fast-decaying T₂-component that originates from water associated with myelin sheaths (17).

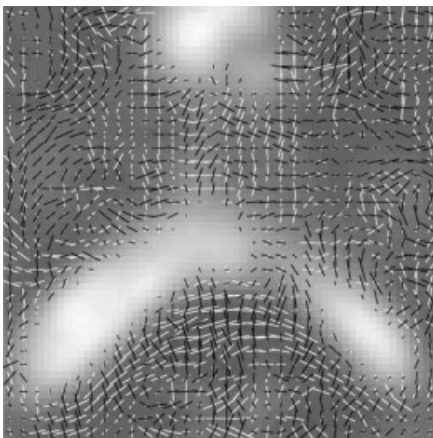


FIG. 3. T₂-weighted subimage of the corpus callosum with the overlaid in-plane component of the first eigenvector of the tensor component sizes, as they are obtained with the unconstrained fitting method. While the eigenvector direction of the fast-diffusion component (white lines) appears to agree with the direction of known fiber structures, the eigenvector direction of the slow-diffusion component (black lines) is seen to be largely orthogonal thereto.

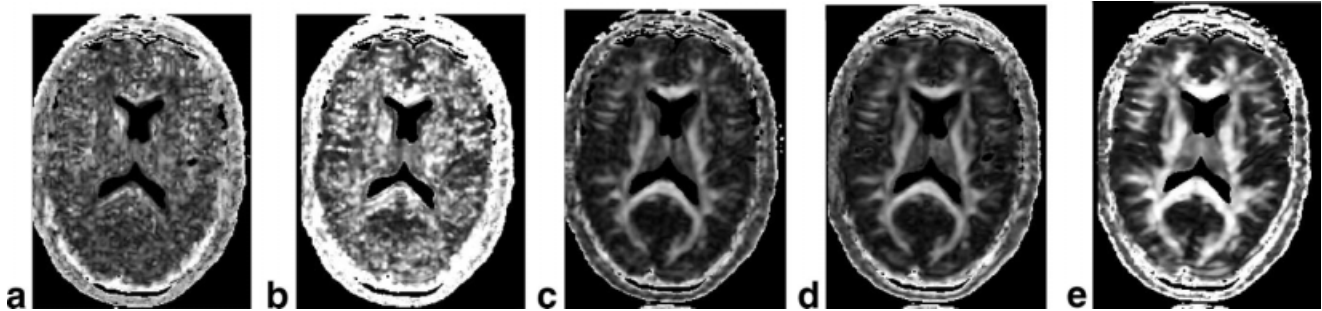


FIG. 4. FA maps of diffusion. All maps are scaled equally, and white corresponds to an FA of one. **a:** Fast-diffusion component FA map of the unconstrained fitting method. **b:** Slow-diffusion component FA map of the unconstrained fitting method. **c:** FA map obtained through monoexponential fitting of a subset of the experiment data, i.e., only the data within a conventional diffusion-weighting range of 5–972 s/mm². **d:** Fast-diffusion component FA map of the constrained fitting method. Note the striking resemblance to the monoexponential FA map. **e:** Slow-diffusion component FA map of the constrained fitting method.

Both of the approaches employed here for data analysis resulted in diffusion tensor data consistent with known fiber anatomy. This is in agreement with previous reports on biexponential diffusion tensor analysis of tissues in vitro. The diffusion tensor study conducted by Elshafiey et al. (10) employed unconstrained component size fits, whereas the studies published by Inglis et al. (9) and Hsu et al. (11), according to personal communications from the first authors of both of these studies, were based on constrained component size fits. It should be added that the simplified fit model applied by Clark et al. (8) can be considered to belong to the unconstrained fit category. The anisotropy of the component sizes that results from unconstrained component size fits has also been noted in earlier studies (3,6,7) that were based on the analysis of only two or three orthogonal diffusion directions. The complete tensor analysis of six independent directions, as set forth in the present study, revealed the orthogonality between the directionally dependent component sizes. At first, this might support the notion of a complex exchange model of two compartments (18), where exchange rates are directionally dependent. On the other hand, tensor component sizes may be the result of the mathematical model chosen, rather than the effect of diffusion in a complex environment.

The slightly smaller average χ^2 error that results from the use of unconstrained rather than constant component

sizes can readily be explained by the larger number of parameters used to fit (i.e., for six diffusion directions, 24 vs. only 14 parameters). On the other hand, while fitting with constant component sizes appears to produce superior anisotropy and eigenvector maps, in areas with very dense fibers the fitting solution generates negative ADC values for the slow-diffusion component. Notably, the negative ADC values occur only along directions with severe diffusion restriction, i.e., orthogonal to the fibers. The negative ADC values along selected directions also explain the occurrence of FA values slightly larger than one (see the corpus callosum values in Table 2). Since negative ADC values have no physical meaning, and they were not observed for unconstrained fits, we considered the possibility that they were an artifact introduced by the initial fit for the determination of the directionally independent component sizes A_f and A_s . In the monoexponential case, fitting of the geometric average of the diffusion-weighted signals along the six directions listed in the Materials and Methods section, does yield correct trace ADC values. In the biexponential case, however, the multiplication of the diffusion-weighted signals, in order to form a composite decay curve, results in cross terms between the exponential functions of the fast- and slow-diffusion components (7), which if neglected may entail incorrect ADC values. With so-called multibranch fitting, a method whereby multiple data sets with common parameters are simultaneously

Table 2

Monoexponential and Biexponential Fractional Diffusion Anisotropy Measured Within Different Regions of Interest in Four Normal Volunteers Biexponential values originate as in Fig. 4 from a fit with constant *component sizes*.

Region of interest	Corpus callosum			Internal capsule			Thalamus		
	FA _m	FA _f	FA _s	FA _m	FA _f	FA _s	FA _m	FA _f	FA _s
Subject 1	0.789	0.794	1.064	0.646	0.647	0.962	0.294	0.307	0.549
Subject 2	0.779	0.786	1.042	0.662	0.676	0.970	0.288	0.244	0.430
Subject 3	0.746	0.771	1.014	0.630	0.643	0.920	0.254	0.267	0.450
Subject 4	0.739	0.721	1.083	0.628	0.651	0.942	0.302	0.280	0.536
Average (N = 4)	0.763	0.773	1.051	0.642	0.654	0.949	0.285	0.275	0.491
SD	0.024	0.024	0.030	0.016	0.015	0.022	0.021	0.026	0.060
Ratio (FA _f or FA _s vs. FA _m)	–	1.013	1.377	–	1.019	1.478	–	0.965	1.723
P (FA _f or FA _s vs. FA _m)	–	N.S.	0.00063	–	N.S.	0.00002	–	N.S.	0.0036

FA_m, monoexponential fractional anisotropy (*b*-factor range of 5 to 972 s/mm²); FA_f, fractional anisotropy of fast diffusion component (*b*-factor range of 5 to 5000 s/mm²); FA_s, fractional anisotropy of slow diffusion component (*b*-factor range of 5 to 5000 s/mm²).

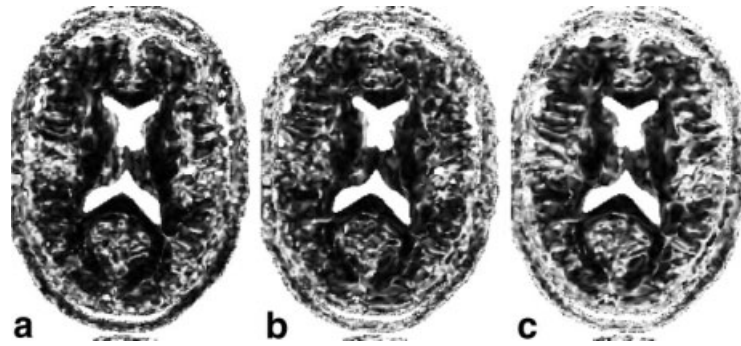


FIG. 5. Angle difference maps of the principal axes of diffusion among the two diffusion components of the biexponential fit, and the single component of the monoexponential fit. The eigenvectors for the fast- and slow-diffusion components are derived from a biexponential fit with directionally independent component sizes. For the monoexponential fit, a subset of data, obtained within a limited b -factor range of 5–972 s/mm^2 , was employed. For improved visualization, deviation angles φ of 90° – 180° were set to the value $180^\circ - \varphi$, and consequently images are scaled from 0° (black) to 90° (white). **a:** Difference between fast and monoexponential components. **b:** Difference between slow and monoexponential components. **c:** Difference between fast- and slow-diffusion components.

fitted by minimizing the total χ^2 error, all parameters can be obtained within a single fit. To verify the validity of the approach used in this study, multibranch fitting was conducted with the Gnuplot software (<http://www.gnuplot.info>) for average signals of an ROI, located in the corpus callosum, where ADC values appeared to be negative. For the diffusion-encoding direction that produced negative values, the average ADC of the slow-diffusion component was $-0.078 \mu m^2/ms$ when component sizes and ADCs were fitted separately, but it was $-0.074 \mu m^2/ms$ when component sizes and ADCs were fitted jointly in a multibranch fit. The differences for the other parameters were equally minor, which seems to support the validity of the approach with separate fitting of component sizes and ADCs.

An interesting finding is the agreement of the FA of the fast-diffusion component and the FA of a monoexponential fit of data obtained within the conventional b -factor range below $1000 s/mm^2$. Also remarkable is the higher FA of the slow-diffusion component. The fact that in more peripheral regions with lower FA, the ratio of FA_s/FA_f increases indicates that the first eigenvector of the slow-diffusion component may permit more detailed and accurate fiber tracking in areas where FA is low, such as in subcortical areas or deep gray matter.

This is the first study to quantitatively compare the directions of the biexponential diffusion eigenvectors in normal human brain. In contrast, to a previous study in heart muscle by Hsu et al. (11), we found that the first eigenvectors of the fast- and slow-diffusion components share the same direction. In addition, we confirmed that this common direction coincides with the direction of the first eigenvector that results from a monoexponential fit of data obtained within the conventional b -factor range below $1000 s/mm^2$. Earlier studies of canine (19) and rabbit (20) heart myocardium, and rat optical tract (21), which used histology or direct tract visualization on MR images, validated the agreement between fiber course and primary diffusion direction derived from a monoexponential fit. The study by Hsu et al. (11) measured the average angle deviation between the first eigenvectors of the two components for the entire heart section, whereas in the current study the average angle deviation was only assessed for small ROIs with high FA or for pixels where the monoexponential FA fell within a certain range. The FA values 0.2 and 0.4 used to define the range limits would constitute cylindrical diffusion with eigenvalue ratios of 1.4/1.0/1.0 and 2.0/1.0/1.0, respectively. Obviously, at lower FA values, noise begins to dominate the sorting of

Table 3

Angle Differences of the Principal Axes of Diffusion Among the Fast and Slow Components of the Biexponential Fit With Constrained Component Sizes and the Single Component of the Monoexponential Fit

Region of interest	φ_{fm} ($^\circ$)	φ_{sm} ($^\circ$)	φ_{fs} ($^\circ$)
Corpus callosum	1.9 (0.2)	3.0 (0.7)	3.7 (1.0)
Internal capsule	1.9 (0.6)	3.2 (0.3)	4.2 (0.6)
Thalamus	8.9 (1.0)	12.3 (2.8)	16.3 (4.3)
σ ($0.4 < FA_m$)	2.5 (0.2)	4.1 (0.4)	4.9 (0.6)
σ ($0.2 < FA_m \leq 0.4$)	5.6 (0.6)	7.6 (0.7)	9.2 (1.0)
δ ($0.4 < FA_m$)	-0.3 (0.1)	-0.4 (0.3)	-0.7 (0.3)
δ ($0.2 < FA_m \leq 0.4$)	-0.7 (0.2)	-0.7 (0.3)	-0.8 (0.3)

φ_{fm} , angle between fast and monoexponential component; φ_{sm} , angle between slow and monoexponential component; φ_{fs} , angle between fast and slow component; σ , SD of adjusted normal distribution; δ , bias of adjusted normal distribution; FA_m , monoexponential fractional anisotropy (b -factor range of 5 to 972 s/mm^2); SD ($N = 4$) is given in parentheses.

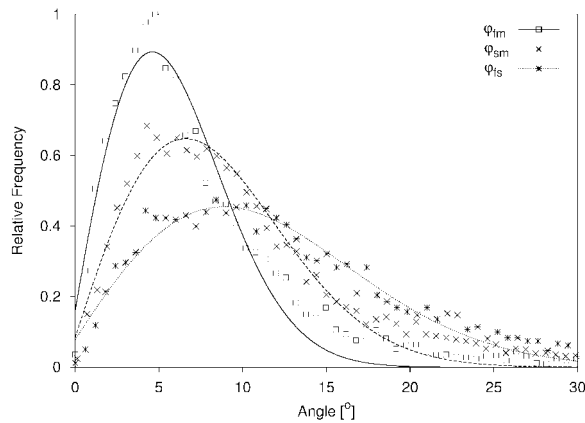


FIG. 6. Example of the distribution and associated fit of deviation angles between the principal axes of diffusion. The histograms include only data from pixels where the FA after monoexponential fitting falls in a range between 0.2 and 0.4. For a detailed explanation of the variables φ_{fm} , φ_{sm} , and φ_{ls} , see Table 3.

eigenvalues, potentially leading to a large incremental deviation between the first eigenvectors. Therefore, it can be assumed that the average deviation angle would have been much higher if the deviation had been measured over the entire brain parenchyma. The results that were obtained through fitting of the distribution of the deviation angle basically confirm the findings made for small ROIs with high and uniform FA. As noted above, it makes sense that the deviation increases with lower FA. The bias δ that was revealed through the fitting of the distribution is very small in comparison with the average deviation φ . Therefore, it can be concluded that for a larger ROI, as defined by the two ranges of FA, the vector field demonstrates no significant bias for any of the components. The consistent negative sign of the computed bias, however, remains unexplained. More-over, this conclusion can not be generalized, since there may be localized deviations that, if averaged over a larger ROI, would increase the SD of the adjusted normal distribution. The proportionality $\varphi_{fm} < \varphi_{sm} < \varphi_{ls}$, which for all ROIs investigated was consistent, indicates that the monoexponential fit exhibits the smallest average deviation between eigenvector and true fiber direction, while the largest deviation results from the slow-diffusion component of the biexponential fit. This

relationship is, at least in part, readily explained by the different component sizes, i.e., on average 100% for the monoexponential fit, and 68% and 32% for the fast- and slow-diffusion biexponential components, respectively (see Table 1).

In the presence of secondary structures, such as secondary nerve fibers penetrating a primary fiber tract (22) or sheets of muscle fibers (23), alignment of the second eigenvector according to the secondary structures can be observed. Evidently the SNR was sufficient to reveal second eigenvector patterns, which could be linked to secondary nerve fibers or sheet-like structures. However, the striking difference in alignment between the juxtacaudate area and the posterior limb of the internal capsule (Fig. 8) is difficult to explain. One can speculate that the observed discrepancy stems from differences in secondary nerve fiber architecture or partial volume effects. Indeed, the juxtacaudate area is known to represent an area of complex and extensive crossings between fibers originating from the nucleus caudatus, the internal capsule, and the corpus callosum.

CONCLUSIONS

To date, the cause for the non-monoexponential diffusion signal decay that is observed in tissues has not been determined. The concept of a two-compartment model, refined by exchange constants, is favored by many authors; however, this remains controversial. It is certainly possible to consider that the fast- and slow-diffusion components represent different compartments, such as the intra-axonal space, the extra-axonal myelin sheath space, and the extracellular space between nerve fibers. All of these compartments exhibit the least restriction along the direction of the fiber and therefore can not be differentiated by the direction of the eigenvector with the largest eigenvalue. For the second eigenvector, two scenarios can be contemplated: In the presence of secondary nerve fibers that pass the primary nerve fibers at an angle close to orthogonal, one would expect that the secondary eigenvector of all compartments aligns according to the direction of the secondary nerve fibers. In the presence of sheet-like structures, however, only the second eigenvector of the extracellular space between nerve fibers would exhibit alignment according to the sheet structure, whereas the

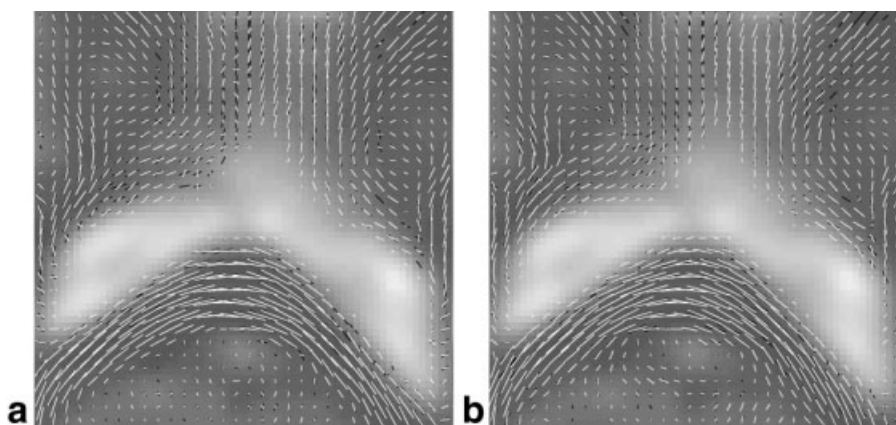
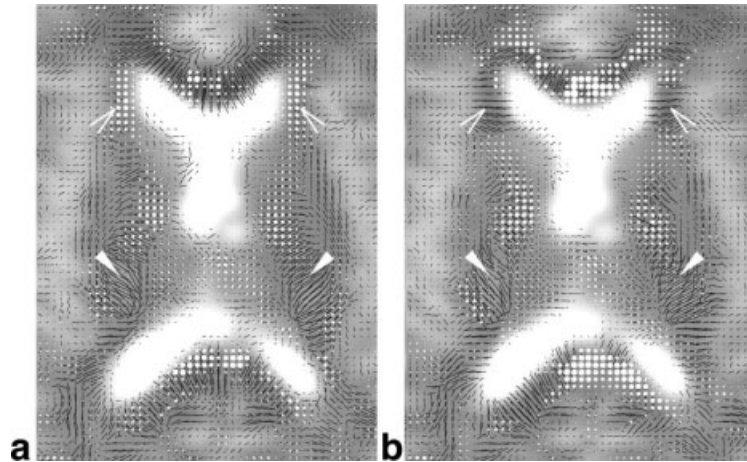


FIG. 7. T_2 -weighted subimages of the corpus callosum with the overlaid in-plane component of the first diffusion eigenvectors. **a:** First eigenvector of the fast-diffusion component of the constrained biexponential fit (white), and the first eigenvector of the monoexponential fit (black). **b:** First eigenvector of the slow-diffusion component of the constrained biexponential fit (white), and the first eigenvector of the monoexponential fit (black). Except for isolated areas, virtually complete agreement between the mono- and biexponential solutions is evident by the covering of white over black lines.

FIG. 8. T_2 -weighted subimages of deep brain structures surrounding the ventricles overlaid with the second diffusion eigenvectors scaled in length by the monoexponential FA value. The in-plane component of the second diffusion eigenvector is represented by black lines, and the out-of-plane component is indicated by white discs that are scaled in size according to the length of the out-of-plane component. The open arrowheads point to the left and right juxtacaudate areas, where fibers originating from the nucleus caudatus, the internal capsule, and the corpus callosum cross. The filled arrowheads designate the left and right posterior limbs of the internal capsule. **a**: Second eigenvector of the fast-diffusion component. **b**: Second eigenvector of the slow-diffusion component. Note the agreement between the fast- and slow-diffusion eigenvector directions in the posterior limb of the internal capsule, and the profound deviation in the anterior limb of the internal capsule.



second eigenvector of the extra-axonal myelin sheath space and the intra-axonal space, in accordance with the cylindrical symmetry of the restriction, would point in random directions. The alignment of the first eigenvectors is well corroborated by the present results. In itself, however, it is not sufficient to prove a connection between observed diffusion components and different compartments at the cellular level. An assessment of the second eigenvector direction was not among the initial aims of the present study, and the findings made at this point must be considered preliminary.

In the first study on biexponential analysis of high b -factor diffusion-weighted signals (1), it was pointed out that the assignment of the components to the extra- and intracellular space based on their diffusion constants leads to relative component sizes that are inconsistent with the respective compartment sizes. Moreover, other studies have found that the two magnetization pools can not be differentiated by T_1 relaxation (24), T_2 relaxation (3), or magnetization transfer (25). These findings do not support the notion of a multicompartiment model, unless moderate exchange between the two magnetization pools is assumed (2, 24). A theoretical paper by Sukstanskii and Yablonskiy (26) proposed that the deviation from a pure monoexponential signal decay may be due to restricted diffusion within a single compartment. However, findings derived from simplified mathematical models may not necessarily be suitable for describing the diffusion tensor in a nerve fiber tract.

The potential clinical value of high- b diffusion-weighted imaging has already been demonstrated in tumors (27–29) and multiple sclerosis (30). While applications for other pathologies are likely to follow, a better understanding and modeling of the underlying biophysics of multiexponential diffusion signal decay will be critical should the technique begin to play a significant role in diagnosis and therapy monitoring. This will also be important in order to define a mathematical model that is free of inconsistencies, some of which were revealed in this study.

ACKNOWLEDGMENT

S.E.M. greatly appreciates the valuable discussions with Spyros Kollias about human brain nerve fiber anatomy.

REFERENCES

- Niendorf T, Dijkhuizen RM, Norris DG, van Lookeren Campagne M, Nicolay K. Biexponential diffusion attenuation in various states of brain tissue: implications for diffusion-weighted imaging. *Magn Reson Med* 1996;36:847–857.
- Mulkern RV, Gudbjartsson H, Westin CF, Zengingonul HP, Gartner W, Guttman CR, Robertson R, Kyriakos W, Schwartz R, Holtzman D, Jolesz FA, Maier SE. Multi-component apparent diffusion coefficients in human brain. *NMR Biomed* 1999;12:51–62.
- Clark CA, Le Bihan D. Water diffusion compartmentation and anisotropy at high b values in the human brain. *Magn Reson Med* 2000;44:852–859.
- Maier SE, Mamata H, Mulkern RV. Biexponential analysis of diffusion related signal decay in human cortical grey matter. In: *Proceedings of the 11th Annual Meeting of ISMRM, Toronto, Canada, 2003*.
- Basser P, Mattiello J, Le Bihan D. MR diffusion tensor spectroscopy and imaging. *Biophys J* 1994;66:259–267.
- Assaf Y, Cohen Y. Assignment of the water slow-diffusing component in the central nervous system using q -space diffusion MRS: implications for fiber tract imaging. *Magn Reson Med* 2000;43:191–199.
- Mulkern RV, Vajapeyam S, Robertson RL, Caruso PA, Rivkin MJ, Maier SE. Biexponential apparent diffusion coefficient parametrization in adult vs newborn brain. *Magn Reson Imaging* 2001;19:659–668.
- Clark CA, Hedehus M, Moseley ME. In vivo mapping of the fast and slow diffusion tensors in human brain. *Magn Reson Med* 2002;47:623–628.
- Inglis BA, Bossart EL, Buckley DL, Wirth ED 3rd, Mareci TH. Visualization of neural tissue water compartments using biexponential diffusion tensor MRI. *Magn Reson Med* 2001;45:580–587.
- Elshafiey I, Bilgen M, He R, Narayana PA. In vivo diffusion tensor imaging of rat spinal cord at 7 T. *Magn Reson Imaging* 2002;20:243–247.
- Hsu EW, Buckley DL, Bui JD, Blackband SJ, Forder JR. Two-component diffusion tensor MRI of isolated perfused hearts. *Magn Reson Med* 2001;45:1039–1045.
- Maier S, Vajapeyam S, Mamata H, Westin CF, Jolesz FA, Mulkern RV. Diffusion tensor imaging of the fast and slow diffusion coefficient components in human brain. In: *Proceedings of the 9th Annual Meeting of ISMRM, Glasgow, Scotland, 2001*.
- Gudbjartsson H, Maier SE, Mulkern RV, Mórocz IÁ, Patz S, Jolesz FA. Line scan diffusion imaging. *Magn Reson Med* 1996;36:509–519.
- Maier SE, Gudbjartsson H, Patz S, Hsu L, Lovblad KO, Edelman RR, Warach S, Jolesz FA. Line scan diffusion imaging: characterization in healthy subjects and stroke patients. *AJR Am J Roentgenol* 1998;17:85–93.
- Mamata H, Mamata Y, Westin CF, Shenton ME, Kikinis R, Jolesz FA, Maier SE. High-resolution line scan diffusion tensor MRI of white matter fiber tract anatomy. *AJNR Am J Neuroradiol* 2002;23:67–75.
- Papadakis NG, Xing D, Houston GC, Smith JM, Smith MI, James MF, Parsons AA, Huang CL, Hall LD, Carpenter TA. A study of rotationally invariant and symmetric indices of diffusion anisotropy. *Magn Reson Imaging* 1999;17:881–892.

17. MacKay A, Whittall K, Adler J, Li D, Paty D, Graeb D. In vivo visualization of myelin water in brain by magnetic resonance. *Magn Reson Med* 1994;31:673–677.
18. Karger J, Pfeiffer H, Heink W. Principles and applications of self-diffusion measurements by NMR. *Adv Magn Reson* 1988;12:1–89.
19. Hsu EW, Muzikant AL, Matulevicius SA, Penland RC, Henriquez CS. Magnetic resonance myocardial fiber-orientation mapping with direct histological correlation. *Am J Physiol* 1998;274(5 Pt 2):H1627–H1634.
20. Scollan DF, Holmes A, Winslow R, Forder J. Histological validation of myocardial microstructure obtained from diffusion tensor magnetic resonance imaging. *Am J Physiol* 1998;275(6 Pt 2):H2308–H2318.
21. Lin CP, Tseng WY, Cheng HC, Chen JH. Validation of diffusion tensor magnetic resonance axonal fiber imaging with registered manganese-enhanced optic tracts. *Neuroimage* 2001;14:1035–1047.
22. Mamata H, Westin CF, De Girolami U, Jolesz FA, Maier SE. Visualization of collateral nerve fibers of human cervical spinal cord: direct histologic validation of diffusion tensor imaging. In: *Proceedings of the 10th Annual Meeting of ISMRM, Honolulu, 2002*.
23. Tseng WY, Wedeen VJ, Reese TG, Smith RN, Halpern EF. Diffusion tensor MRI of myocardial fibers and sheets: correspondence with visible cut-face texture. *J Magn Reson Imaging* 2003;17:31–42.
24. Mulkern RV, Zengingonul HP, Robertson RL, Bogner P, Gudbjartsson H, Guttman CR, Holtzman D, Kyriakos W, Jolesz FA, Maier SE. Multi-component apparent diffusion coefficients in human brain: relationship to spin-lattice relaxation. *Magn Reson Med* 2000;44:292–300.
25. Mulkern RV, Vajapeyam S, Maier SE. Magnetization transfer studies of the fast and slow apparent diffusion coefficient (ADC) components in the human brain. In: *Proceedings of the 9th Annual Meeting of ISMRM, Glasgow, Scotland, 2001*.
26. Sukstanskii A, Yablonskiy D. Effects of restricted diffusion on MR signal formation. *J Magn Reson* 2002;157:92–105.
27. Maier SE, Bogner P, Bajzik G, Mamata H, Mamata Y, Repa I, Jolesz FA, Mulkern RV. Normal brain and brain tumor: multicomponent apparent diffusion coefficient line scan imaging. *Radiology* 2001;219:842–849.
28. Maier SE, Mamata H, Mulkern RV. Characterization of normal brain and brain tumor pathology by chi squares parameter maps of diffusion-weighted image data. *Eur J Radiol* 2003;45:199–207.
29. Mardor Y, Pfeffer R, Spiegelmann R, Roth Y, Maier SE, Nissim O, Berger R, Glicksman A, Baram J, Orenstein A, Cohen JS, Tichler T. Early detection of response to radiation therapy in patients with brain malignancies using conventional and high b-value diffusion weighted MRI. *J Clin Oncol* 2003;21:1094–1100.
30. Assaf Y, Ben-Bashat D, Chapman J, Peled S, Biton IE, Kafri M, Segev Y, Hendler T, Korczyn AD, Graif M, Cohen Y. High b-value q-space analyzed diffusion-weighted MRI: application to multiple sclerosis. *Magn Reson Med* 2002;47:115–126.